

Molecular and colloidal transport in bacterial cellulose hydrogels

Firoozeh Babayekhorasani, Maryam Hosseini, and Patrick T. Spicer*

School of Chemical Engineering, University of New South Wales, Sydney, NSW, Australia

E-mail: p.spicer@unsw.edu.au

Phone: +61 2 9385 5744

Abstract

Bacterial cellulose biofilms are complex networks of strong interwoven nanofibers that control transport and protect bacterial colonies in the film. Design of diverse applications of these bacterial cellulose films also relies on understanding and controlling transport through the fiber mesh, and transport simulations of the films are most accurate when guided by experimental characterization of the structures and the resultant diffusion inside. Diffusion through such films is a function of their key microstructural length scales, determining how molecules, as well as particles and microorganisms, permeate them. We use microscopy to study the unique bacterial cellulose film via its pore structure and quantify the mobility dynamics of various sizes of tracer particles and macromolecules. Mobility is hindered within the films, as confinement and local movement strongly depend on the void size relative to diffusing tracers. The biofilms have a naturally periodic structure of alternating dense and porous layers of nanofiber mesh, and we tune the magnitude of the spacing via fermentation conditions. Micron-sized particles can diffuse through the porous layers, but can not penetrate the dense layers. Tracer mobility in the porous layers is isotropic, indicating a largely random pore structure there. Molecular diffusion through the whole film is only slightly reduced by

the structural tortuosity. Knowledge of transport variations within bacterial cellulose networks can be used to guide the design of symbiotic cultures in these structures and enhance their use in applications like biomedical implants, wound dressings, lab-grown meat, clothing textiles, and sensors.

keywords

cellulose hydrogels, diffusion, microscopy, confined mobility, biofilms

Introduction

Bacterial cellulose is produced in a film at the air-liquid interface of *Acetobacter xylinum* cultures that transform aqueous sugar into balsamic vinegar and kombucha^{1,2}, but the cellulose itself is an active area of exploration by researchers. In contrast with biofilms based on cell-produced exopolysaccharides (EPS), here bacteria build a network of pure cellulose fibers of nanometer-scale thickness and micron-scale lengths intertwined in a mesh structure, or pellicle: a stable living environment for symbiotic cultures of bacteria and yeast (SCOBY).³ Bacterial cellulose biofilms are remarkably strong⁴ versus the softer biofilms made of EPS, prompting their study for use as packaging⁵, biomedical implants⁶⁻⁸, wound dressings⁹⁻¹¹, sensors¹², batteries^{13,14}, food¹⁵⁻¹⁷, clothing^{18,19} and lab-grown meat²⁰. All of these applications benefit from a complex cellulose fiber mesh providing mechanical strength, low density, and high surface area, but their performance is determined by the transport properties inside the mesh²¹. Modifying the pore size of the film or surface properties of the cellulose nanofibers, for example, could enhance cell retention and adherence for lab-grown meat production²⁰. In order to accurately design and simulate²² materials made from bacterial cellulose films, a careful characterization of their structure and transport properties is needed, and that is the focus of this work.

In random fiber networks, mesh size, alignment and heterogeneity can lead to strong

variations in microparticle transport rates²³⁻²⁵ and localization^{26,27}. Particle dynamics are coupled to any spatial heterogeneity of the matrix²⁸, for example, affecting drug transport in cancer tissue^{23,29} as well as the movement of soft particle medical delivery vehicles³⁰⁻³². Complex biological network structures can vary significantly³³, but diffusive transport can be measured in the matrix via molecular or colloidal tracer studies³⁴⁻³⁸. Diffusive transport in EPS biofilm networks has been studied to measure how rheology^{39,40}, diffusive permeability^{41,42}, and restructuring modulate transport in the matrix^{43,44}, but cellulose biofilms have not been characterized in the same way. In this study, we use optical microscopy to track molecular and particulate⁴⁵ tracers to characterize mobility within anisotropic, hierarchically structured bacterial cellulose films and show the diversity of natural structures and properties found there.

We find bacterial cellulose films naturally exhibit strong periodic variations in fiber packing density over micron-scale distances, alternating between porous layers that are permeable to cells or colloids and dense layers that are impermeable to all but molecular transport. We tune the overall density of the films by adjusting the viscosity of the growth medium, demonstrating its effects on diffusive transport. Diffusion of colloidal tracer particles in the films depends on their size relative to the fiber mesh dimensions and heterogeneity. Mean squared displacement of a range of particle sizes is sub-diffusive and non-Gaussian in the films, and the transition from diffusive to anomalous sub-diffusive behavior is determined by the size of the particle relative to the mesh void space and the time scale of interaction. We also observe that the diffusive dynamics of macromolecules are mostly isotropic in the films, despite the random fiber structure. Understanding transport within bacterial cellulose films is necessary to enable rational design and simulation of myriad biomedical and synthetic materials, as they all depend on transport of molecules, particles, or microorganisms through their structures for viability and performance.

Experimental

Preparation of the bacterial biofilms

Acetobacter xylinum was provided by Nourishme Organics, Australia, and used to grow the pellicles. The culture medium was prepared by seeping black tea into boiling water for 10 minutes. Sucrose solutions at 10 % w/v were added to the tea solution.

The culture medium was then mixed with aqueous sodium alginate solution of different concentrations to make the final concentration of the cultures between 0 - 1 % w/v. The culture medium was incubated at 25 °C for 10 days. Cellulose fibers formed in the culture and moved to the air-liquid interface. As more fibers forms, the thickness of the layer at the interface increases. After 10 days, the consolidated films were collected from the interface. The film was carefully washed using DI water to remove bacteria and any loosely attached fibrous material from the films. The films were washed in 0.5 M NaOH (Chem-Supply Pty Ltd, Australia) at 90 °C for 90 minutes to kill the remaining bacteria. The films were then washed with water until neutralized. The washed films were immersed in an aqueous solution of 1.5 % w/v methylchloroisothiazolinone preservative (Sigma Aldrich, Sydney, Australia) and stored at 4 °C before the microscopy experiments.

Characterization of the bacterial biofilms

The structure of the biofilms is characterized using scanning electron microscopy (SEM), confocal, and light-sheet microscopy techniques. Samples are freeze-dried overnight and imaged from the side interface using a field-emission scanning electron microscope (NanoSEM 230).

The side interface of the wet samples is also imaged using a ZEISS Light-sheet Z.1 microscope with a 20× water immersion objective (NA=1.0). To image the samples using the light-sheet microscope, the biofilms are first stained using 0.5 % w/v Congo Red dye (Sigma Aldrich, Sydney, Australia) and incubated for 15 minutes. The samples are cut into

small rectangular cubes with dimensions of roughly $1\text{ mm} \times 5\text{ mm} \times$ the film height. The samples are placed inside PTFE tubing with a matched refractive index to water. The tube is filled with deionized (DI) water. Both ends of the tube are sealed with PARAFILM (Sigma Aldrich, Sydney, Australia). The tube is then connected to a syringe and is loaded inside the microscope chamber. A thin section of the sample is imaged by illuminating from the left and right sides. The two sides are then combined using an automated dual side fusion method by ZEN Black software.

Preparation of tracer particle dispersions in the biofilms

Polybead carboxylate green dyed microspheres with diameter of $0.20\ \mu\text{m}$, $0.50\ \mu\text{m}$, and $1\ \mu\text{m}$ at a concentration of 2.5 % were purchased from Polyscience, Inc (Warrington, PA, USA) and were diluted using DI water, $1000\times$, $500\times$, and $200\times$, respectively. The homogenized particle suspension is added to the films that are already stained with Congo red dye (0.5 % w/v) and incubated overnight to allow particle diffusion through the biofilm matrix.

Imaging of the tracer particles diffusing through the biofilms

The samples were imaged using a light-sheet microscope equipped with a $20\times$ water immersion objective of numerical aperture $\text{NA}=1.0$ with a frame rate of 5 fps from the side interface. To ensure the particles are diffusing through the biofilm, we imaged both the biofilm matrix and the particles simultaneously using two separate channels. We acquired time-series images of different locations through the depth of the side interface of the biofilms. We acquired 1000 images over time with pixel size of $3.94\ \text{pix}/\mu\text{m}$ and image size of $487 \times 487\ \mu\text{m}^2$. We used single-particle tracking algorithm⁴⁵ to locate and track the particles over time. Using particle trajectories, we calculated the ensemble average mean squared displacement, $\Delta x^2(\Delta t) = \langle (x(t + \Delta t) - x(t))^2 \rangle$, over lag time, Δt .

Fluorescence Recovery After Photo-bleaching (FRAP) analysis

Recovery of the intensity of fluorescein isothiocyanate–dextran (FITC-Dextran) with three molecular weights of 4, 20, 40 kDa was measured using Zeiss LSM 880 (JENA/Germany) confocal microscopes. The film is first cut into a regular shape with dimensions of $5 \times 5 \times 2 \text{ mm}^3$ from the side interface of the full film. The Congo Red labeled film was incubated in 1 mg/ml of FITC-Dextran solutions for 24 hr under gentle agitation. The film is imaged using a 40X water immersion objective (NA=1.1). The selected area is then bleached for about 2–3 sec and imaged over 1000 frames to follow the recovery of intensity with a frame rate of 30 fps.

Results and discussion

Cellulose biofilms are formed during static growth of *Acetobacter xylinum* in an aqueous culture, as the cellulose fibers gradually combine and move up to the liquid-air interface. Over time, more fibers grow and join the layer on the top and produce a consolidated pellicle film (Figure 1a). The film is an entangled network of cellulose fibers, seen when the structure is imaged from its top or bottom interface (Figure 1b). The network shows a distinct degree of structural periodicity when observed from its side (Figure 1 c.1–c.3) where dense layers of fibers alternate with more porous regions of random fibrous mesh (Figure 1 c.1–c.3). The regions are all sufficiently porous to allow nutrient transfer through the biofilm, but the denser intermediate layers are likely to restrict the diffusion of most particles or cells³⁴. The periodic fiber density gradient is fairly typical of cellulose films^{46–49}, and is likely a result of periods of surface drying and fiber consolidation as well as different bacterial growth patterns⁵⁰.

The periodic variation in film permeability and transport creates a complex pathway for diffusing species and likely aids in protection of the bacteria, but we are not aware of specific evolutionary benefits. The overall fiber density of the mesh can also be controlled,

if needed, in applications requiring different microstructures and pore accessibility^{51,52}. One method of control is to increase the viscosity of the culture medium by adding thickeners like sodium alginate,⁵³⁻⁵⁵ that reduce bacterial mobility throughout the culture medium. As the medium viscosity increases in the culture, the thickness of the film and the spacing between the periodic layers decreases (Figure 1 d.1–d.3). Interestingly, the mass of cellulose produced does not change significantly. This indicates the growth rate of cellulose is unchanged, but the mobility of the bacteria is expected to be decreased by the increased viscosity. As a result, the bacteria do not spread out as widely but still grow the same amount of cellulose, resulting in thinner and denser films. To some extent the spacing between the periodic layers and the overall porosity of the film can be controlled by tuning the viscosity and movement of the bacteria in the culture. The stark difference wrought by addition of the thickener is easily demonstrated by comparing the films grown without sodium alginate, Figure 1c, and with 1% *w/v* sodium alginate, Figure 1d. The native structure in Figure 1c has periodic dense layers with regular spacing of around 60 μm while the structure in Figure 1d has a layer spacing nearly 6 \times smaller. The two biofilms contain the same mass of cellulose, but their varied structures result in respective bulk fiber densities of only 0.01 g/cm^3 and 0.03 g/cm^3 based on dry weight and wet volume measurements. The results in Figure 1 demonstrate that we can control the physical spacing and relative distance within these periodic fiber structures to understand and control diffusive transport effects. Below we study the effects of the varied spacing and pore size distribution on directional transport using particle tracking.

We study the mobility of tracers that range from macromolecular to colloidal length scales, 2 nm – 1 μm , because the two different films have pores that span similar dimensions. Combined light-sheet and confocal microscopy techniques enable structural quantification of large biological samples^{50,56} and single particle tracking⁴⁵. Fluorescence Recovery After Photobleaching (FRAP) resolves molecular-scale transport within the overall network. As the cellulose fibers are strongly interwoven in the mesh due to hydrogen bonding, they won't

be able to move or fluctuate noticeably. Imaging the stained fibers simultaneously with particles over time did not show any movement by fibers over the course of the experiments.

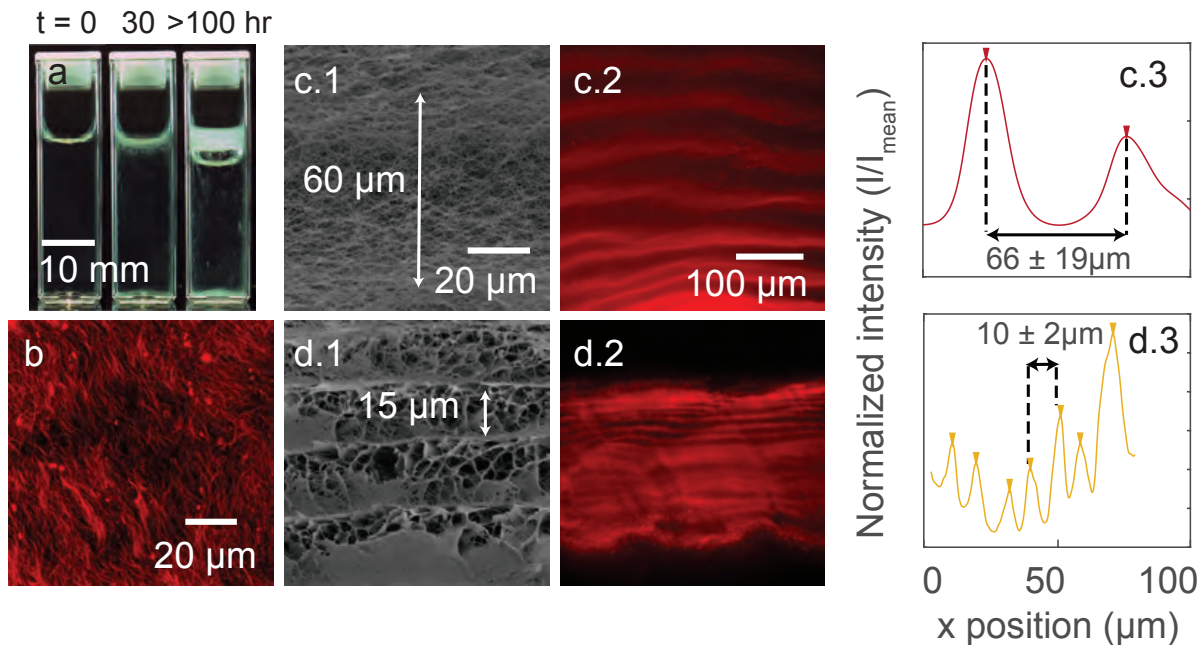


Figure 1: Macro and microstructure of the cellulose pellicle film. a) A cellulose biofilm forms as a white layer at the top of a cuvette during bacterial production of nanofibers. b) Microstructure of the film imaged from the top interface. c) SEM images (c.1), light-sheet micrograph (c.2) and intensity profile measured from the light-sheet image (c.3) of the side of the film grown in the media with no sodium alginate. d) SEM images (d.1), light-sheet micrograph (d.2) and intensity profile measured from the light-sheet image (d.3) of the side of the film grown in the media with 1 % *w/v* of sodium alginate. The unique periodic spacing of denser layers within the overall fiber mesh structure is visible from the side interface.

We first investigate the effect of colloidal tracer size on diffusive mobility within a native film. A representative light-sheet image of tracer particles with diameter of 0.5 μm reveals that particles are well-dispersed within the porous layers of the native film (Figure 2a.1). The embedded tracer particles within the films are monodisperse and remain monodisperse during the experiment though their shape can appear a bit distorted by the combination of the two beams used to create the light-sheet⁵⁷, Figure 2a.1. We further confirm the tracers remain monodisperse in the films with confocal microscopy images in Figure 2a.2. The colloidal particles can only diffuse within the porous layers because the pore opening of the

dense layers is smaller than all of the tracer particle sizes used, schematically illustrated in Figures 2b.1–b.3.

The mean-squared displacement (MSD) of the tracers significantly decreases as the particle size increases in both the biofilm and in water (Figure 2c), consistent with the reduced diffusivity of larger colloids. Mobility inside the film, Figure 2c, symbols, is noticeably smaller than in water, Figure 2c dashed lines, for all three tracer sizes because of the physical confinement by the fiber mesh. The MSD of particles inside the film grows more slowly, when compared to the free diffusion of the particles in water, and plateaus at longer lag times, Figure 2c. The power-law exponent of the MSD for all three particles in the film as a function of time is smaller than one ($MSD \sim t^\alpha$, $\alpha < 1$), indicating confined mobility and sub-diffusive dynamics within the network.

We scaled the MSD of each tracer size by that of the largest tracer particle diameter, $d_1 = 1 \mu\text{m}$, to distinguish between the effects of film confinement and tracer particle size on mobility. The scaling causes perfect overlap of the data for tracers in water, bold dashed line in Figure 2d, and eliminates variations in mobility due to particle size, symbols in Figure 2d. The scaling also indicates the fluid in the film has the viscosity of water and any hindered mobility is due to confinement effects. The scaling also allows us to see how film confinement affects tracer mobility, Figure 2d. The average pore size of the porous layers of the native film is $0.5 - 1 \mu\text{m}$, and we can use this information to anticipate transport within the network.

Here, within the time frame of the experiment, particles with diameter of $1 \mu\text{m}$ are mostly confined by the network, as the local cages never disentangle. Smaller particles with diameters of $0.2 \mu\text{m}$ and $0.5 \mu\text{m}$ are also partially hindered due to the network heterogeneity. Particles can freely diffuse within larger pores, but remain partially or permanently trapped within the smaller pores and exhibit sub-diffusive motion at short time scales. Increasing tracer particle diameter then also increases the degree of sub-diffusive transport within the fiber mesh. The sub-diffusive exponent of particles of different sizes, estimated from the slope of the logarithmic mean-squared displacement, decreases as the particle size increases

(Figure 2d, inset), and particles slow down as a result of increased encounters with bounding fibers (Table S2). Similar to our observation, confined mobility of particles in a cross-linked polymeric network is sub-diffusive ($\alpha = 0.5$) for time lags smaller than the relaxation time of a polymer chain⁵⁸. At larger time scales, particles are trapped and the MSD approaches a plateau.

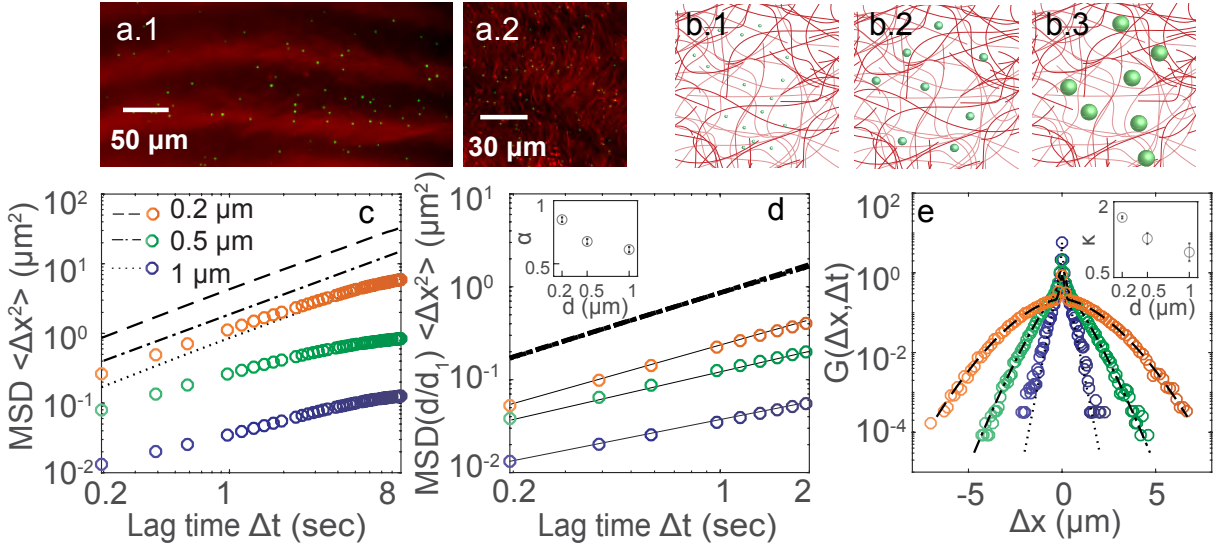


Figure 2: Particle mobility is increasingly hindered within the cellulose film as the particle size increases. a.1) Image of the native film from the side interface with $0.5 \mu\text{m}$ particles embedded inside captured by light-sheet microscopy. a.2) Image of the native film from the top interface with $0.5 \mu\text{m}$ particles embedded inside captured by confocal microscopy. b.1–b.3) Schematics of the particles with different sizes, $0.2 \mu\text{m}$ (b.1), $0.5 \mu\text{m}$ (b.2), and $1 \mu\text{m}$ (b.3) diffusing in the film grown with no alginate (native film). Ensemble average mean squared displacement, MSD (c), scaled mean squared displacement (d), and distributions of particle displacements at $\Delta t = 2 \text{ s}$ (e) of the particles with diameter of $0.2 \mu\text{m}$ inside the film (orange circle) and in water (dashed line), of $0.5 \mu\text{m}$ inside the film (green circle) and in water (dash dotted line), and of $1 \mu\text{m}$ inside the film (purple circle) and in water (dotted line). Inset in (d) plots the sub-diffusive exponent (α) as a function of tracer particle diameter and inset in (e) plots the stretching exponent (κ) as a function of tracer particle diameter.

The distribution of particle displacements measured at $\Delta t = 2 \text{ s}$ is plotted in Figure 2e. Two distinct populations are noted for all particle sizes. One population, at the center of the distribution near $\Delta x = 0$, can be attributed to nearly immobile particles. The second, broader population is the mobile or partially mobile particles at higher magnitude Δx values,

Figure 2e. The different populations can be described by fitting the distribution of particle displacements to a sum of a Gaussian function and a stretched exponential function^{59,60} expressed as:

$$G_s(\Delta x, \Delta t) = a_1 \exp\left(-\left(\frac{\Delta x}{\delta}\right)^2\right) + a_2 \exp\left(-\left|\frac{\Delta x}{\gamma(\Delta t)}\right|^\kappa\right)$$

The Gaussian function fits the center of the distribution, quantifying the trapping of some particles within very small pores of the heterogeneous film. The stretched exponential tail of the distribution, on the other hand, characterizes the particles that are moving within the pore space and are only partially hindered by pore wall confinement. The stretched exponential fit provides a value of the stretching exponent, κ , that quantifies the confinement effects on mobility and deviations from Gaussian particle diffusion. As the particle size increases, the stretching exponent decreases as we see in Figure 2e, inset. The stretching exponent of the particles with diameter of 0.2 μm is close to the Gaussian value, $\kappa = 2$, while the value for the particles with diameter of 1 μm is close to $\kappa = 1$ (Figure 2e, inset), indicating deviation from Gaussian dynamics for the larger tracer particles. The dynamics of the mobile, and partially mobile, particles are also governed by particle size. For particle diameters more than five times smaller than the average pore size, movement is not confined within the voids.

Dynamical heterogeneity in other soft glassy systems leads to a non-Gaussian distribution of displacements, where the motion is decoupled into fast and slow populations during the structural relaxation^{28,60,61}. Entrapped particles within the structure form a Gaussian center and free particles form an exponential tail of the distribution, just as we see here. Diffusion of particles within actin filament solutions^{62,63}, through cells⁶⁴, and within colloidal suspensions^{61,65} is also observed to be non-Gaussian due to the spatiotemporal heterogeneity of the environment, where the elasticity of the structure controls the behaviour of the sub-populations. Non-Gaussian behaviour is observed because individual particles have het-

erogeneous dynamics temporally along their movements and spatially compared to other particles, where series of Gaussian events with changing variance lead to observation of exponential behavior⁶⁶.

Here, subdivision of the particle displacements into the slow and fast dynamics mostly reflects the spatial heterogeneity of the underlying fiber mesh structure, producing clear non-Gaussian behaviour. The heterogeneous mobility of particles trapped within pores of different sizes creates a series of Gaussian distributions with different variance for the mobile populations forming the tail. The collective distribution of all the events is therefore non-Gaussian⁶⁶ and the stretching exponent shows the degree of variability of the distributions of the mobile population.

Dynamics of the tracer particles with diameters of 0.2 μm and 1 μm are next compared in two films with different overall fiber mesh densities. The native film has a bulk fiber density of 0.01 g/cm^3 while the compact film has a density of 0.03 g/cm^3 . A light-sheet micrograph of the native film is shown in Figure 3a.1, formed with no alginate present, and a more compact film in Figure 3a.2 formed with 1 % w/v of sodium alginate present. Trajectories of the 0.2 μm and 1 μm exhibit a pronounced difference in the native (Figure 3a.3, top row) and the compact (Figure 3a.3, bottom row) biofilms. To eliminate the effect of particle size, particle trajectories are colored based on the value of their normalized diffusivity, $D(d/d_1)$. Trajectories of particles with diameter of 0.2 μm are essentially free to diffuse with only intermittent hindrance. Particles with diameter of 1 μm , however, follow trajectories with longer intervals of slowed mobility. The representative trajectories show reduced diffusivity when the particle size increases or when the density of the network increases. To quantify the effect of mesh density on tracer mobility, the MSD and the distribution of particle displacements are compared for mobility of particles within different films.

The MSD of the tracers with diameter of 0.2 μm in the native film is about five times smaller than for diffusion in water. Diffusion in the alginate-grown compact film is also reduced by a factor of two compared to the native film and by a factor of 10 compared to

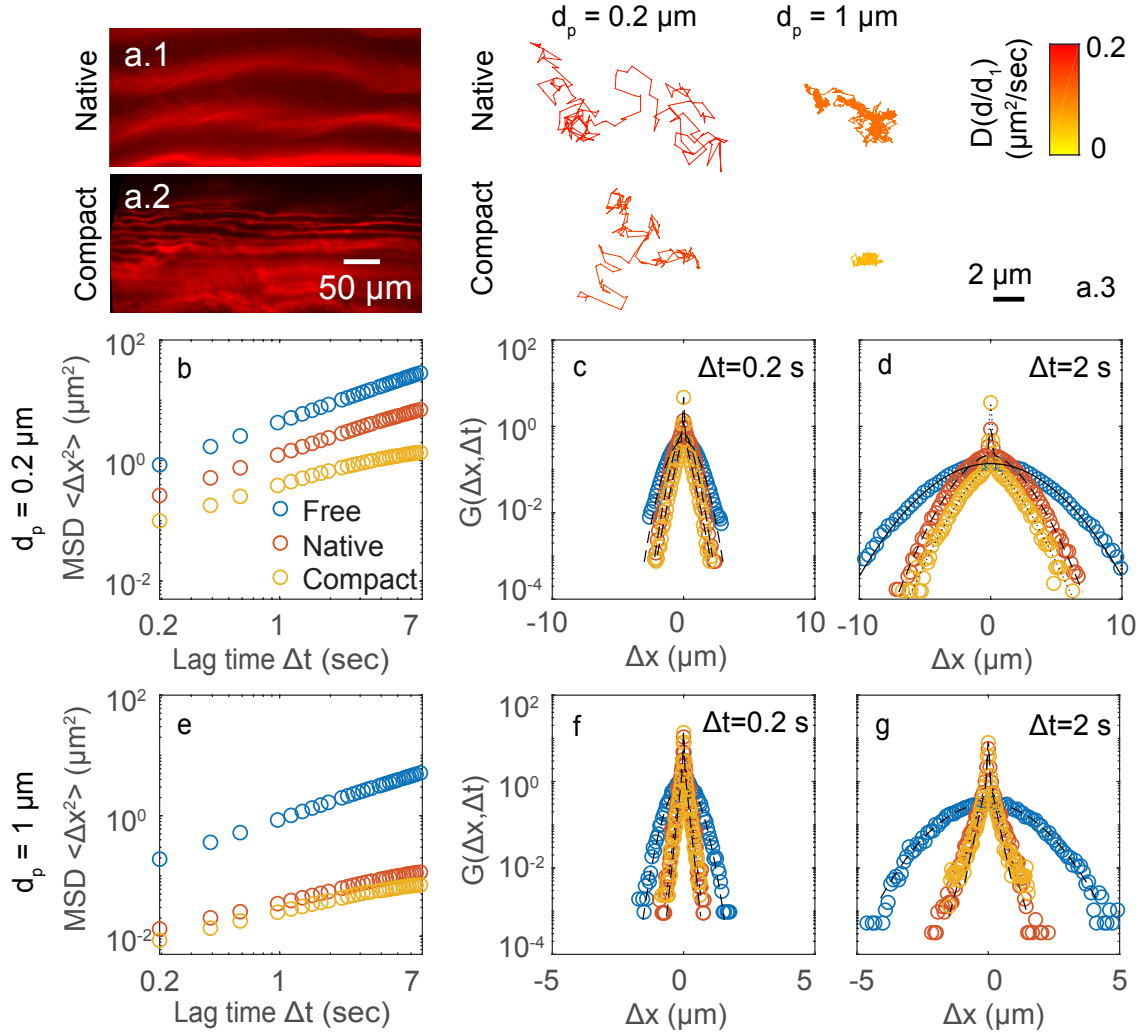


Figure 3: Tracers dynamics vary in different spatial structures. Micro-structure of native (a.1) and compact (a.2) films. Representative trajectories (a.3) of the particles of different sizes (0.2 and 1 μm) diffusing in the native (a.1) and the compact (a.2) films. The color shows the normalized average diffusion coefficient of the trajectories. b) Mean squared displacement, c) distributions of particle displacements at $\Delta t=0.2$ s and d) at $\Delta t=2$ s of particles of 0.2 μm diffusing in water (blue circle), in the native films (red circle), and in the compact film (yellow circle). e) Mean squared displacement, f) distributions of particle displacements at $\Delta t=0.2$ s and g) at $\Delta t=2$ s of particles of 1 μm diffusing in water (blue circle), in the native film (red circle), and in the compact film (yellow circle).

free aqueous diffusion (Table S2). The slope of the logarithmic MSD at short times ($\Delta t < 5$ s) decreases from 1 in water to ~ 0.9 in the native film and to ~ 0.7 in the compact film (Figure 3b). The difference in the microstructure of the two biofilms (Figure 1 c and d) can be assessed based on the degree of hindrance of particles with the same size in each film. Reduced MSD and increased sub-diffusivity of $0.2 \mu\text{m}$ particles in the compact film indicates the local pores, on average, confine particles to a greater extent.

The distribution of particle displacements, represented at $\Delta t = 0.2$ and 2 s (Figure 3 c – d), also signifies the difference between hindered mobility within the native and compact films. The distribution of particle displacements exhibits a slightly narrower tail within the films compared to the distribution within water and also forms two populations of displacements. The difference is more visible at longer time lags ($\Delta t = 2$ s), when the average particle displacement increases and particles more frequently encounter the fiber mesh (Figure 3 d and g). Here, the tails of the distributions are significantly narrower within the films, indicating reduced mobility at longer time lags. The difference in the behavior of the mobile population of particles within the two films reveals that even local displacements are controlled by the ratio of the particle to void diameter (Figure 3 d and g).

The MSD of $1 \mu\text{m}$ tracers decreases by more than one order of magnitude in both film types, compared to the dynamics in water, and is slightly smaller in the compact than the native film (Figure 3e). The slope of the logarithmic MSD is also reduced from 1 in water to ~ 0.6 in the native and compact films. Similar to what is observed in the dynamics of $0.2 \mu\text{m}$ tracers, the width of the distribution of particle displacements with diameter of $1 \mu\text{m}$ reduces within the two films and the difference is more obvious at longer time lags. The distributions of particle displacements within the two films, however, nearly overlap at short and long time lags. The mobility of the $1 \mu\text{m}$ particles is strictly hindered within the films, where the particle diameter is close to the average mesh pore size and the dynamics are not significantly affected by the mesh heterogeneity (Figure 3 f and g), because both are confining. The dynamics of the $0.2 \mu\text{m}$ tracers seem to be more sensitive to the change in

the structure of the films and the confinement effect on the reduced mobility of the $0.2\ \mu\text{m}$ tracers in the compact film is much greater. The temporal trajectories of single-particle displacements (Figure S1) show that mobile particles have random displacement till they disappear from the imaging volume. The average residence time of the particles increases as particle size increases. The immobile particles remain mostly stationary throughout the imaging sample time. However, a small portion of the immobile particles ($\approx 5\%$) infrequently jump from their cages. The waiting time between the jumps depends on the ratio of the particle to the cage size and spans from short to long times because of the pore heterogeneity.

We calculate the MSD of single $0.2\ \mu\text{m}$ and $1\ \mu\text{m}$ tracers to obtain more insight into individual tracer size effects on movement within the films. The logarithmic MSD of the individual particles in both native and compact films is more widely distributed than the MSD of single particles in water (Figure 4a, b, e, and f). We classify the individual MSDs with large varieties into two categories of immobile and mobile, using thresholds of $0.1\ \mu\text{m}^2$ for the $0.2\ \mu\text{m}$ tracers and $0.01\ \mu\text{m}^2$ for the $1\ \mu\text{m}$ tracers, based on the crossover point between the two populations at $\Delta t = 2\ \text{s}$. (Figure 2d and g).

The categorized MSDs illustrate the effect of the underlying biofilm structure on the local mobility of single tracer particles and the two film types show distinct behavior for the $0.2\ \mu\text{m}$ tracers. The single MSDs of the mobile category have greater overlap with the MSDs of the particles in water (Figure 4a), indicating the presence of more particles with unconfined motions in the native film. The immobile category of the particles within the compact film has larger population with smaller mobility compared to the immobile category in the native film. The structure of the native film has, on average, less confining effect than the compact film on the mobility of the $0.2\ \mu\text{m}$ tracers (Figure 4a and b). Increased tracer size removes these distinctions, as the mobile and immobile categories of the $1\ \mu\text{m}$ tracers are very similar in the native and the compact films. The mobility of the mobile or partially mobile category of all tracer trajectories is smaller than the mobility of particles in water. (Figure 4e and f). The observations indicate the compact film's small pores limit the mobility of both $0.2\ \mu\text{m}$

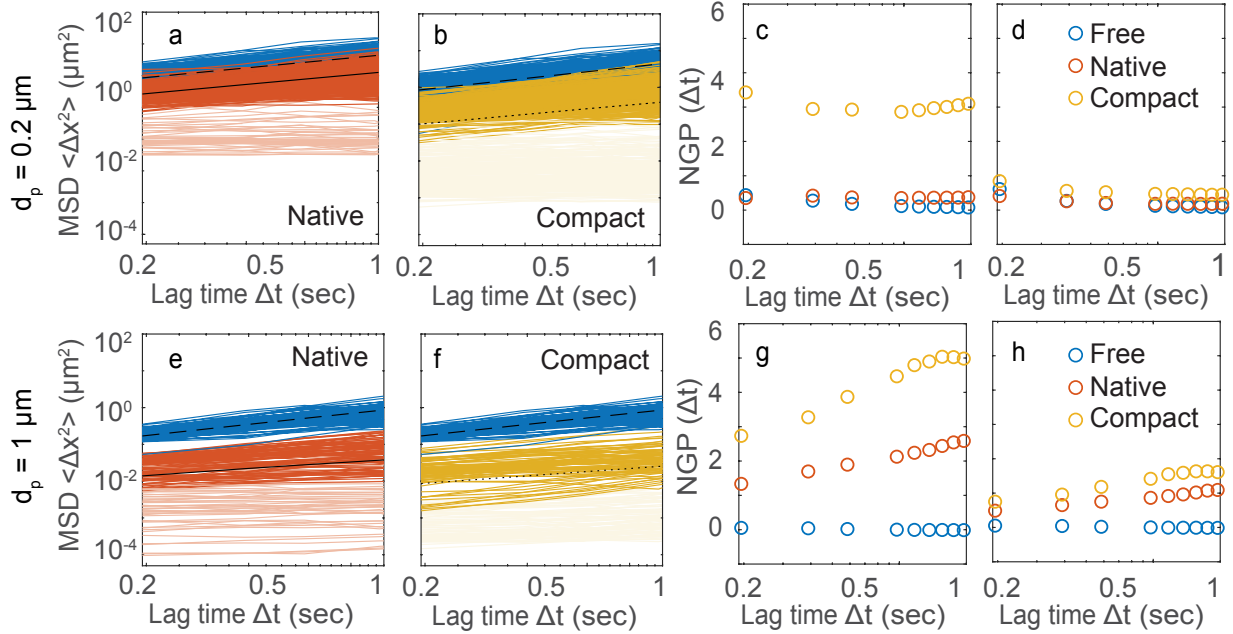


Figure 4: Individual tracers experience different levels of confinement within the heterogeneous films. Mean squared displacement of single $0.2 \mu\text{m}$ particles diffusing in the native film, classified in two groups of mobile (dark red lines in a) and immobile (light red lines in a) and in the compact film, classified in two groups of mobile (dark yellow lines in b) and immobile (light yellow lines in b). Blue lines in a and b show free diffusion of $0.2 \mu\text{m}$ tracers and black dashed lines show the ensemble MSD. Non-Gaussian parameters of all tracers (c) and only mobile $0.2 \mu\text{m}$ tracers (d) diffusing in water (blue circle), in the native films (red circle), and in the compact films (yellow circle). Mean squared displacement of single $1 \mu\text{m}$ tracers diffusing in the native biofilm, classified into groups of mobile (dark red lines in e) and immobile (light red lines in e) and in the compact biofilm, classified into groups of mobile (dark yellow lines in f) and immobile (light yellow lines in f). Blue lines in e and f show free diffusion of $1 \mu\text{m}$ tracers in water and black dashed lines show the ensemble MSD. Non-Gaussian parameters of all tracers (g) and (h) only mobile $1 \mu\text{m}$ tracers diffusing in water (blue circle) and in the native (red circle), and in the compact (yellow circle) films. Black lines in a and e show the ensemble MSD of $0.2 \mu\text{m}$ and $1 \mu\text{m}$ tracers in the native film and black dotted lines in b and f show the ensemble MSD of $0.2 \mu\text{m}$ and $1 \mu\text{m}$ tracers in the compact film.

and 1 μm tracers, meaning we can control biofilm transport rates across length scales relevant to colloidal and bacterial diffusion.

The non-Gaussian parameter⁶⁷, $\alpha(\Delta t) = ((\langle \Delta x^4 \rangle) / (3 \langle \Delta x^2 \rangle^2) - 1)$, over time quantifies the effects of confinement on the immobile tracers identified earlier. The α of the total population of 0.2 μm tracers is slightly greater than zero in the native film, but notably larger in the compact film (Figure 4c) and increases over time as mobility becomes more hindered. For the mobile sub-population of the 0.2 μm particles, however, the non-Gaussian parameter is closer to zero within the native and the compact film. Removing the immobile population from the displacements of the 0.2 μm tracers reduces the non-Gaussian parameter to near zero for all times (Figure 4d). Dynamic heterogeneity, however, produces a measurable non-Gaussian parameter for the mobile sub-population of 0.2 μm tracers within the compact film.

The estimated non-Gaussian parameter of the 1 μm tracers is non-zero in both native and compact films for the total tracer population and is larger in the compact film (Figure 4g), quantifying the effects of the two films' different pore size distributions. Here removing the immobile sub-population reduces the non-Gaussian parameter, indicating the mobile population diffusion is also quite non-Gaussian in the biofilms (Figure 4h). Even though the 1 μm tracers are mobile within the two films, their movements are heterogeneous and non-Gaussian.

Quantifying the percentage of particles that are immobile and mobile provides insight to differentiate the pore characteristics of the network. The immobile tracers are hindered in their motion by pores that are similar in size to the particles. This explanation is supported by the fact that the percentages of immobilized tracers increase as the size of the pore and the tracer particle change and become more similar. Comparing the percentage of the mobile and the immobile particles of different sizes in the native film shows that as particle size increases, the percentage of immobile particles within the film increases. For the 0.2 μm tracers within the native film, only 5% of the particles are immobile, while the percentage of

immobile 0.5 and 1 μm particles increases to 10% and 37%, respectively, within the native film. This indicates the existence of small pores with diameter of 0.5 – 1 μm , limiting the mobility of particles with a size greater than 0.5 μm . The percentage of immobile particles in the compact film is larger compared to the percentage in the native film. The difference is more significant for the 0.2 and 0.5 μm tracers and is 29% and 23%, respectively. For the 1 μm particles, half (49%) remain mostly immobile. The compact film, on average, thus has smaller pores, about 0.2 – 0.5 μm , compared to the native film, and hinders the mobility of particles with smaller sizes.

Previous work²³ has identified strongly anisotropic diffusive mobility in fiber matrices and the film studied here might be expected to exhibit similar effects. We assess diffusive mobility of 0.2 μm and 0.5 μm particles in the horizontal/parallel and vertical/perpendicular directions of the native film as a means of quantifying any anisotropic transport. Micron-sized particles can only diffuse in the low-density regions of the films between the dense layers so those results are the focus here (Figure 5a).

The long-time trajectories of particles exhibit a more horizontally dominated movement, parallel to the typical void orientation (Figure 5b). The MSD of the 0.2 μm particles is 1.4 \times greater in the parallel direction than the perpendicular direction, (Figure 5c). The difference is more evident in the MSD of 0.5 μm particles (Figure 5d). The mobility of the larger 0.5 μm particles is more limited so the effect of structural orientation of the media on mobility of the particles is stronger, 1.6 \times (Figure 5d).

The distribution of the particle displacements also confirms that particles tend to diffuse slightly faster through the direction parallel to the horizontally-oriented pores (Figure 5e and f). The biofilm is formed and thickened at the air-liquid interface, where bacteria are largely constrained to two-dimensional, lateral movement. As a result, the intermediate densified layers are formed from a horizontally-aligned network of fibers (Figure 5g.1). The porous layers between the dense layers have more random fiber orientation, (Figure 5g.3 and g.5).

A 2D fast Fourier transform (2D-FFT) analysis of the confocal images of the dense and

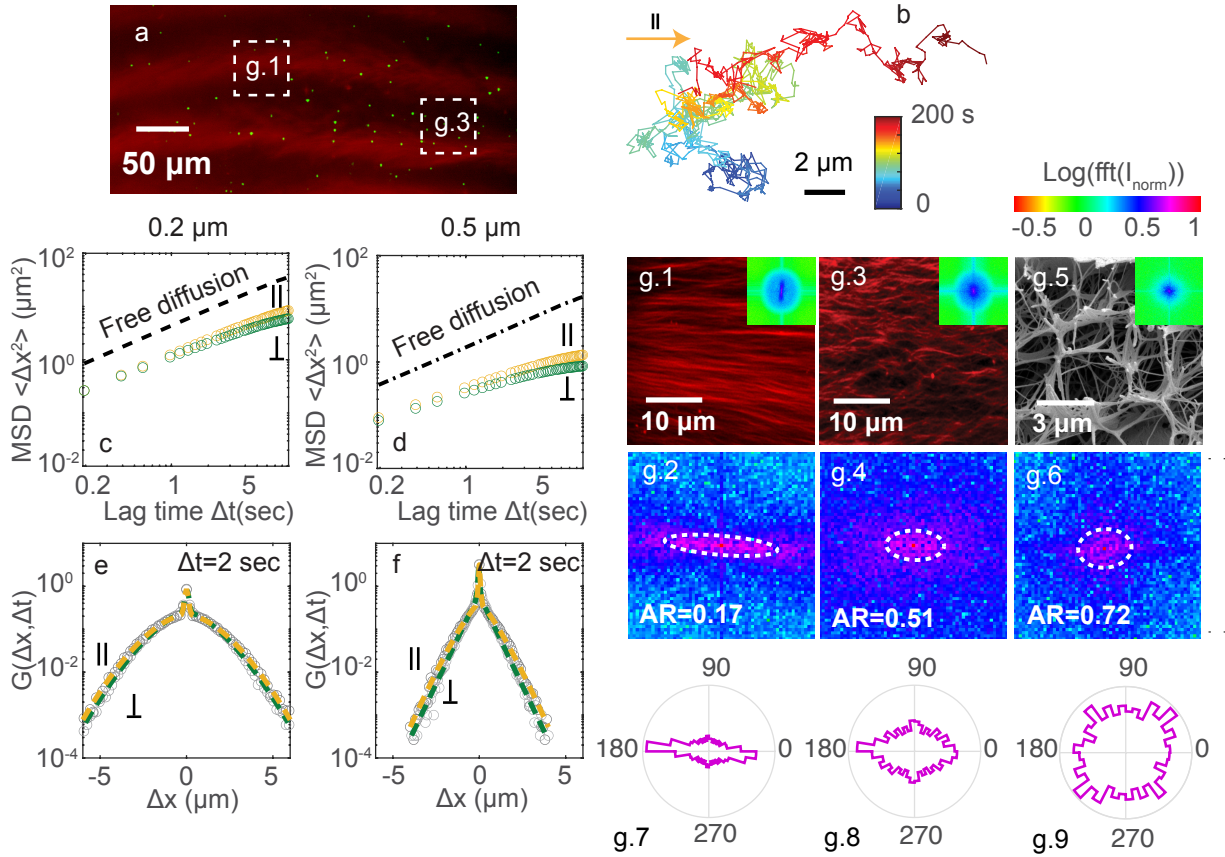


Figure 5: The structural orientation of the film influences dynamics of the tracer particles in the x and y directions. a) Structure of the native film from the side interface with 0.5 μm diameter particles diffusing in the layers. b) A representative trajectory of a 0.5 μm particle in the native film. The color bar represents the diffusion time of the particle. Ensemble average mean squared displacements of (c) 0.2 μm and (d) 0.5 μm particles in the horizontal and vertical directions in the film. Distribution of particle displacements of (e) 0.2 μm and (f) 0.5 μm particles at $\Delta t = 2$ sec for horizontal and vertical mobility. The magnified confocal images from the layer (g.1) the interlayer locations (g.3) and the SEM image of the interlayer location (g.5). The inset represents 2D-FFT images of each location. The magnified images of the low spatial frequencies shifted by 90 degree for the confocal-layer (g.2) and the confocal-interlayer (g.4) and the SEM-interlayer (g.6). The polar distribution of radially integrated angles for the layer (g.7) and the interlayer (g.8) and the SEM-interlayer (g.9) depict degree of alignment of the fibers in the horizontal directions. Color bar of the 2D-FFT images represents logarithmic power spectrum values of the normalized intensity of the images.

porous layers, inset of 5g.1 and g.3, and the SEM image of the porous layer, inset of 5g.5, quantify the structural anisotropy. The magnified low spatial frequencies of the 2D-FFT images, shifted by 90° , are aligned in the parallel direction (Figure 5g.2, g.4, and g.6). The center of the power spectrum is fitted to an ellipse and the ratio of the minor to major axis length is defined as the directionality aspect ratio, AR ⁶⁸. The smaller the AR , the more fibers are aligned, with the dense layer exhibiting an $AR = 0.17$. Confinement anisotropy reduces significantly within the porous layer with $AR = 0.72$. Distribution of the fiber angle orientation is calculated from the radially-integrated value of the 90° -shifted power spectrum at each angle (Figure 5g.7 – g.9). The polar distribution of angles, in agreement with the estimated AR , indicates a reduced confinement anisotropy for the fibers in the porous layers. Particle tracking at different length scales also confirms that, although mobility is slightly hindered in the perpendicular direction, confinement anisotropy within the porous region is minimal.

The periodic structure of the biofilms results from the regular formation of dense, more consolidated layers of fibers with an average 2D fiber fraction of $64 \pm 5\%$, measured from the confocal images (Figure 6 a and b.1). The porous layers between the dense layers have a lower fiber area density of $42 \pm 4\%$ (Figure 6 a and c.1). Tracer particles with diameters between $0.2 \mu\text{m}$ and $1 \mu\text{m}$ can only diffuse within the porous layers and can not penetrate the dense layers of either film, Figure 5a, though macromolecules can.

The barrier properties of the dense layers are assessed by measuring molecular diffusion of fluorescein isothiocyanate-dextran (FITC–dextran) with molecular weights between 4 and 40 kDa using Fluorescence Recovery After Photobleaching (FRAP). Selected areas inside, Figure 6 b.2 – b.4, and between, Figure 6 c.2 – c.4, the dense layers were studied to provide an overall characterization of the composite film. During recovery, fluorescent dye diffused back into the circular bleached region, and the normalized fluorescent intensity is calculated as $I_{norm}(t) = \frac{I(t) - I_{bleach}}{I_{pre} - I_{bleach}}$, where $I_{norm}(t)$ is the normalized intensity, $I(t)$ is the intensity of the bleached area over time during recovery, I_{bleach} is the average bleached intensity, and

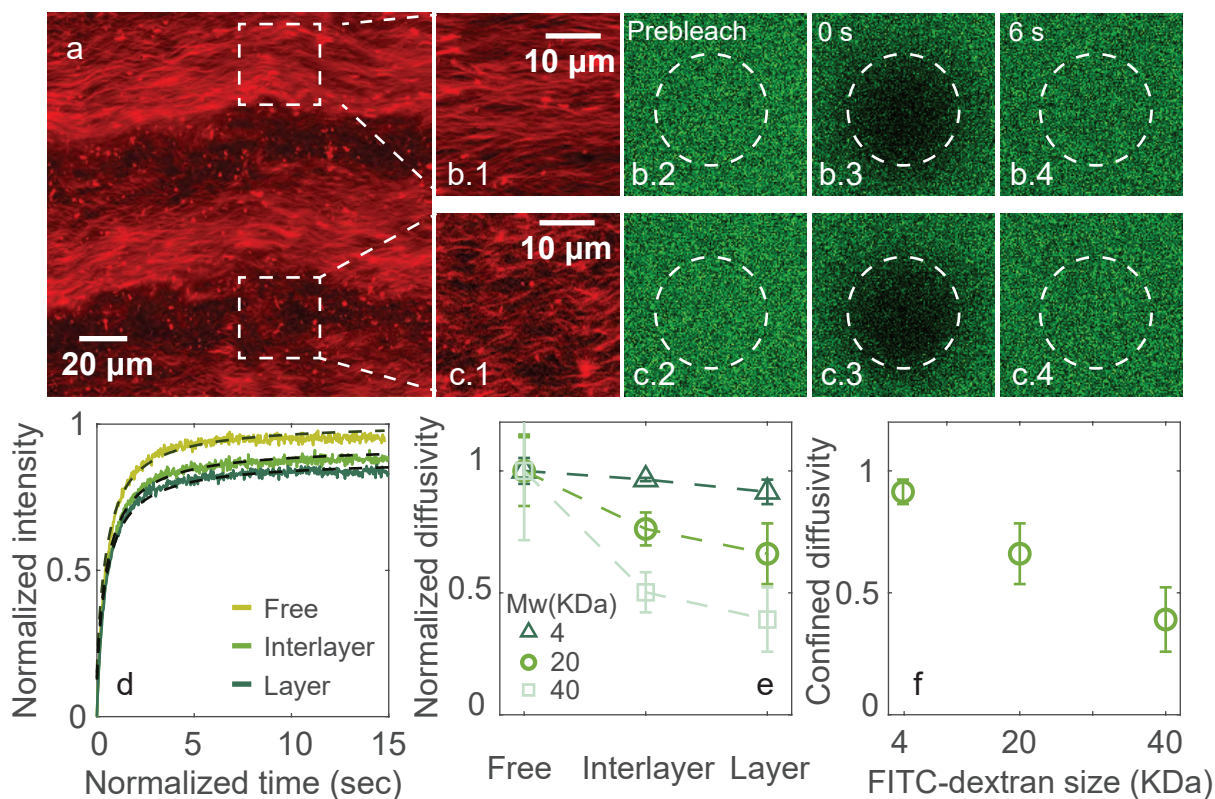


Figure 6: Molecular mobility is reduced as FITC-dextran diffuses through the biofilm. a) Confocal image of the biofilm side interface highlights the layered microstructure of the film. b,c) Zoomed-in images of the structure in a (b.1) porous and (c.1) dense layer. Intensity of FITC-dextran (20 kDa) (b.2 and c.2) prior to bleaching, (b.3 and c.3) just after bleaching, and (b.4 and c.4) after recovery at $t = 6$ s for selected locations inside and between dense layers. d) Normalized intensity of FITC-dextran (20 kDa) over time for recovery after bleaching within water (light green), the porous layer (medium green) and the dense layer (dark green) with the fitted model. e) Average normalized diffusivity (D/D_{free}) of FITC-dextran with different molecular weights (4 - 40 kDa) in different areas. f) Confined normalized diffusivity (D/D_{free}) within the dense layers for FITC-dextran of different molecular weights.

I_{pre} is the average intensity before bleaching. The recovery of the normalized intensity is fitted to $I_{norm}(t) = A.e^{-2\tau_D/t} \left(I_0(2\tau_D/t) + I_1(2\tau_D/t) \right)$ assuming lateral diffusion within the film, where A is the pre-exponential factor and τ_D is the half time recovery of the normalized intensity⁶⁹. The diffusion coefficient can be estimated as $D = 0.88w^2/4\tau_D$ for a circular bleached area with a radius of w ⁷⁰. Diffusive mobility of 4 kDa FITC–dextran is not hindered within the porous and the dense layers of the biofilm compared to the free diffusive mobility. Increasing the FITC–dextran molecular weight to 20 and 40 kDa, however, reduces the average diffusivity.

The diffusive dynamics are more confined (reduced by ~ 25 %) inside the dense layers, Figure 6e, and the confined mobility, on average, decreases as the FITC–dextran size increases, Figure 6f and Table S3. The behavior is consistent with the observed hindered dynamics of micron-size tracer particles in the film. The heterogeneous structure of the biofilm contains a wide distribution of pore sizes. While the average pore size of the network ($0.5 - 1 \mu\text{m}$) is much larger than the size of the FITC–dextran molecules, the molecular mobility is still hindered $2\times$, meaning that network connectivity and heterogeneity can also affect the molecular diffusion in the film. Similar confined mobility was previously measured for protein secretion and diffusion of macromolecules within hydrogel networks^{71–74}.

Conclusions

Transport within bacterial cellulose biofilms is a phenomenon central to many applications of the unique fiber mesh material, as well as design and simulation of these materials, whether the goal is diffusion of nutrients, cells, or ions. We might naively assume these films have an entirely random fiber structure, but show using microscopy that the films have periodic structures of very dense oriented fiber layers alternating with more porous random fiber layers. Particle tracking provides an excellent measure of the complex, anisotropic pore structures within the fiber network as an indicator of specific performance parameters like

mesh size, pore diameter, and permeability. Complementary confocal and light-sheet microscopy techniques enable assessment of the effects of process fermentation conditions and provide a means of specifying the performance needed for various applications.

The spatially varying packing density of the bacterial cellulose biofilms presents a complex pathway for diffusing particles, where the relative tracer particle diameter and network structure control the mobility. As these dimensions can radically alter accessibility of the film by entities of certain sizes, we demonstrate that the overall compactness of the film can be controlled during its growth by adding sodium alginate to thicken the culture medium.

The MSD of particles with varying sizes is sub-diffusive and non-Gaussian in the biofilms, with the level of sub-diffusivity increasing as the particle size increases or the compactness of the network increases. Consequently, tracer trajectories vary significantly depending on relative dimensions. Mobility at different length scales in the film is slightly more hindered in the direction perpendicular to the predominant fiber growth direction. Distinctive dynamics of the particles in different media can be utilized to probe the underlying structure of the biofilms. Understanding the pronounced structural variation of complex fibrous networks over micron length scales could enhance the accuracy of efforts to design synthetic tissue scaffolds, for example, or improve modeling²³ of transport of nutrients or antibiotics within fibrous biofilms.

Supporting Information Available

MSD cutoff; Temporal trajectories; Diffusivity of tracers and macromolecules within the native film and the compact film; Diffusivity of tracers and macromolecules within the native film and the compact film

Acknowledgement

Light-sheet and confocal microscopy and scanning electron microscopy were performed using

instruments situated in, and maintained by, the Katharina Gaus Light Microscopy Facility (KGLMF) and Electron Microscope Unit (EMU) at the Mark Wainwright Analytical Centre, UNSW Sydney. MH acknowledges a UNSW Scientia Fellowship. Partial support from ARC DP190102614 is gratefully acknowledged.

Bibliography

- (1) Soares, M. G.; de Lima, M.; Schmidt, V. C. R. Technological aspects of kombucha, its applications and the symbiotic culture (SCOBY), and extraction of compounds of interest: A literature review. *Trends Food Sci. Technol.* **2021**, *110*, 539–550.
- (2) Chakravorty, S.; Bhattacharya, S.; Chatzinotas, A.; Chakraborty, W.; Bhattacharya, D.; Gachhui, R. Kombucha tea fermentation: Microbial and biochemical dynamics. *Int. J. Food Microbiol.* **2016**, *220*, 63–72.
- (3) Rooney, L. M.; Amos, W. B.; Hoskisson, P. A.; McConnell, G. Intra-colony channels in *E. coli* function as a nutrient uptake system. *ISME J.* **2020**, *14*, 2461–2473.
- (4) Tanpichai, S.; Quero, F.; Nogi, M.; Yano, H.; Young, R. J.; Lindström, T.; Sampson, W. W.; Eichhorn, S. J. Effective young’s modulus of bacterial and microfibrillated cellulose fibrils in fibrous networks. *Biomacromolecules* **2012**, *13*, 1340–1349.
- (5) Shi, Z.; Zhang, Y.; Phillips, G. O.; Yang, G. Utilization of bacterial cellulose in food. *Food hydrocolloids* **2014**, *35*, 539–545.
- (6) Bangasser, B. L.; Shamsan, G. A.; Chan, C. E.; Opoku, K. N.; Tüzel, E.; Schlichtmann, B. W.; Kasim, J. A.; Fuller, B. J.; McCullough, B. R.; Rosenfeld, S. S., et al. Shifting the optimal stiffness for cell migration. *Nat. Commun.* **2017**, *8*, 1–10.
- (7) Witzler, M.; Alzagameem, A.; Bergs, M.; Khaldi-Hansen, B. E.; Klein, S. E.;

- Hielscher, D.; Kamm, B.; Kreyenschmidt, J.; Tobiasch, E.; Schulze, M. Lignin-derived biomaterials for drug release and tissue engineering. *Molecules* **2018**, *23*, 1885.
- (8) Yamada, K. M.; Sixt, M. Mechanisms of 3D cell migration. *Nat. Rev. Mol. Cell Biol.* **2019**, *20*, 738–752.
- (9) Markstedt, K.; Mantas, A.; Tournier, I.; Martínez Ávila, H.; Hägg, D.; Gatenholm, P. 3D bioprinting human chondrocytes with nanocellulose–alginate bioink for cartilage tissue engineering applications. *Biomacromolecules* **2015**, *16*, 1489–1496.
- (10) Curvello, R.; Raghuwanshi, V. S.; Garnier, G. Engineering nanocellulose hydrogels for biomedical applications. *Adv. Colloid Interface Sci.* **2019**, *267*, 47–61.
- (11) Ahmed, J.; Gultekinoglu, M.; Edirisinghe, M. Bacterial cellulose micro-nano fibres for wound healing applications. *Biotechnol. Adv.* **2020**, *41*, 107549.
- (12) Gilbert, C.; Tang, T.-C.; Ott, W.; Dorr, B. A.; Shaw, W. M.; Sun, G. L.; Lu, T. K.; Ellis, T. Living materials with programmable functionalities grown from engineered microbial co-cultures. *Nat. Mater.* **2021**, *20*, 691–700.
- (13) Chen, C.; Hu, L. Nanocellulose toward Advanced Energy Storage Devices: Structure and Electrochemistry. *Acc. Chem. Res.* **2018**, *51*, 3154–3165.
- (14) Kim, J. H.; Lee, D.; Lee, Y. H.; Chen, W.; Lee, S. Y. Nanocellulose for Energy Storage Systems: Beyond the Limits of Synthetic Materials. *Adv. Mater.* **2019**, *31*, 1–16.
- (15) Schaffner, M.; Rühs, P. A.; Coulter, F.; Kilcher, S.; Studart, A. R. 3D printing of bacteria into functional complex materials. *Sci. Adv.* **2017**, *3*, eaao6804.
- (16) Hausmann, M. K.; Ruhs, P. A.; Siqueira, G.; Lauger, J.; Libanori, R.; Zimmermann, T.; Studart, A. R. Dynamics of cellulose nanocrystal alignment during 3D printing. *ACS Nano* **2018**, *12*, 6926–6937.

- (17) Joshi, S.; Cook, E.; Mannoor, M. S. Bacterial Nanobionics via 3D printing. *Nano Lett.* **2018**, *18*, 7448–7456.
- (18) Quijano, L.; Speight, R.; Payne, A. Future fashion, biotechnology and the living world: Microbial cell factories and forming new ‘oddkins’. *Continuum* **2021**, *35*, 897–913.
- (19) da Silva, C. J. G.; de Medeiros, A. D.; de Amorim, J. D. P.; do Nascimento, H. A.; Converti, A.; Costa, A. F. S.; Sarubbo, L. A. Bacterial cellulose biotextiles for the future of sustainable fashion: a review. *Environ. Chem. Lett.* **2021**, *19*, 2967–2980.
- (20) Rybchyn, M. S.; Biazik, J. M.; Charlesworth, J.; le Coutre, J. Nanocellulose from Nata de Coco as a Bioscaffold for Cell-Based Meat. *ACS Omega* **2021**, *6*, 33923–33931.
- (21) Witten, J.; Ribbeck, K. The particle in the spider’s web: transport through biological hydrogels. *Nanoscale* **2017**, *9*, 8080–8095.
- (22) Stylianopoulos, T.; Yeckel, A.; Derby, J. J.; Luo, X.-J.; Shephard, M. S.; Sander, E. A.; Barocas, V. H. Permeability calculations in three-dimensional isotropic and oriented fiber networks. *Phys. Fluids* **2008**, *20*, 123601.
- (23) Stylianopoulos, T.; Diop-Frimpong, B.; Munn, L. L.; Jain, R. K. Diffusion anisotropy in collagen gels and tumors: The effect of fiber network orientation. *Biophys. J.* **2010**, *99*, 3119–3128.
- (24) Sykes, E. A.; Dai, Q.; Sarsons, C. D.; Chen, J.; Rocheleau, J. V.; Hwang, D. M.; Zheng, G.; Cramb, D. T.; Rinker, K. D.; Chan, W. C. Tailoring nanoparticle designs to target cancer based on tumor pathophysiology. *Proc. Natl. Acad. Sci. U. S. A.* **2016**, *113*, E1142–E1151.
- (25) Chauhan, V. P.; Stylianopoulos, T.; Boucher, Y.; Jain, R. K. Delivery of molecular and nanoscale medicine to tumors: transport barriers and strategies. *Annu. Rev. Chem. Biomol. Eng.* **2011**, *2*, 281–298.

- (26) Sentjabrskaja, T.; Zaccarelli, E.; De Michele, C.; Sciortino, F.; Tartaglia, P.; Voigtmann, T.; Egelhaaf, S. U.; Laurati, M. Anomalous dynamics of intruders in a crowded environment of mobile obstacles. *Nat. Commun.* **2016**, *7*, 1–8.
- (27) Poling-Skutvik, R.; Roberts, R. C.; Slim, A. H.; Narayanan, S.; Krishnamoorti, R.; Palmer, J. C.; Conrad, J. C. Structure dominates localization of tracers within aging nanoparticle glasses. *J. Phys. Chem. Lett.* **2019**, *10*, 1784–1789.
- (28) Roberts, R. C.; Poling-Skutvik, R.; Conrad, J. C.; Palmer, J. C. Tracer transport in attractive and repulsive supercooled liquids and glasses. *J. Chem. Phys.* **2019**, *151*, 194501.
- (29) Jain, R. K.; Stylianopoulos, T. Delivering nanomedicine to solid tumors. *Nat. Rev. Clin. Oncol.* **2010**, *7*, 653–664.
- (30) Yu, M.; Xu, L.; Tian, F.; Su, Q.; Zheng, N.; Yang, Y.; Wang, J.; Wang, A.; Zhu, C.; Guo, S., et al. Rapid transport of deformation-tuned nanoparticles across biological hydrogels and cellular barriers. *Nat. Commun.* **2018**, *9*, 1–11.
- (31) Yu, M.; Song, W.; Tian, F.; Dai, Z.; Zhu, Q.; Ahmad, E.; Guo, S.; Zhu, C.; Zhong, H.; Yuan, Y.; Zhang, T.; Yi, X.; Shi, X.; Gan, Y.; Gao, H. Temperature- and rigidity-mediated rapid transport of lipid nanovesicles in hydrogels. *Proc. Natl. Acad. Sci. U. S. A.* **2019**, *116*, 5362–5369.
- (32) Bao, C.; Liu, B.; Li, B.; Chai, J.; Zhang, L.; Jiao, L.; Li, D.; Yu, Z.; Ren, F.; Shi, X.; Li, Y. Enhanced transport of shape and rigidity-tuned α -Lactalbumin nanotubes across intestinal mucus and cellular barriers. *Nano Lett.* **2020**, *20*, 1352–1361.
- (33) Huck, B. C.; Hartwig, O.; Biehl, A.; Schwarzkopf, K.; Wagner, C.; Loretz, B.; Murgia, X.; Lehr, C. M. Macro- and microrheological properties of mucus surrogates in comparison to native intestinal and pulmonary mucus. *Biomacromolecules* **2019**, *20*, 3504–3512.

- (34) Birjiniuk, A.; Billings, N.; Nance, E.; Hanes, J.; Ribbeck, K.; Doyle, P. S. Single particle tracking reveals spatial and dynamic organization of the *Escherichia coli* biofilm matrix. *New J. Phys.* **2014**, *16*, 085014.
- (35) Billings, N.; Birjiniuk, A.; Samad, T. S.; Doyle, P. S.; Ribbeck, K. Material properties of biofilms—a review of methods for understanding permeability and mechanics. *Rep. Prog. Phys.* **2015**, *78*, 036601.
- (36) Mastorakos, P.; Silva, A. L.; Chisholm, J.; Song, E.; Choi, W. K.; Boyle, M. P.; Morales, M. M.; Hanes, J.; Suk, J. S. Highly compacted biodegradable DNA nanoparticles capable of overcoming the mucus barrier for inhaled lung gene therapy. *Proc. Natl. Acad. Sci. U. S. A.* **2015**, *112*, 8720–8725.
- (37) Marczynski, M.; Käs Dorf, B. T.; Altaner, B.; Wenzler, A.; Gerland, U.; Lieleg, O. Transient binding promotes molecule penetration into mucin hydrogels by enhancing molecular partitioning. *Biomater. Sci.* **2018**, *6*, 3373–3387.
- (38) Dunsing, V.; Irmischer, T.; Barbirz, S.; Chiantia, S. Purely polysaccharide-based biofilm matrix provides size-selective diffusion barriers for nanoparticles and bacteriophages. *Biomacromolecules* **2019**, *20*, 3842–3854.
- (39) Stewart, E. J.; Ganesan, M.; Younger, J. G.; Solomon, M. J. Artificial biofilms establish the role of matrix interactions in staphylococcal biofilm assembly and disassembly. *Sci. Rep.* **2015**, *5*, 1–14.
- (40) Ganesan, M.; Knier, S.; Younger, J. G.; Solomon, M. J. Associative and entanglement contributions to the solution rheology of a bacterial polysaccharide. *Macromolecules* **2016**, *49*, 8313–8321.
- (41) Kundukad, B.; Schussman, M.; Yang, K.; Seviour, T.; Yang, L.; Rice, S. A.; Kjelleberg, S.; Doyle, P. S. Mechanistic action of weak acid drugs on biofilms. *Sci. Rep.* **2017**, *7*, 1–12.

- (42) Boudarel, H.; Mathias, J.-D.; Blaysat, B.; Grédiac, M. In situ tracking of microbeads for the detection of biofilm formation. *Biotechnol. Bioeng.* **2021**, *118*, 1244–1261.
- (43) Chew, S. C.; Kundukad, B.; Seviour, T.; Van der Maarel, J. R.; Yang, L.; Rice, S. A.; Doyle, P.; Kjelleberg, S. Dynamic remodeling of microbial biofilms by functionally distinct exopolysaccharides. *MBio* **2014**, *5*, e01536–14.
- (44) Kundukad, B.; Seviour, T.; Liang, Y.; Rice, S. A.; Kjelleberg, S.; Doyle, P. S. Mechanical properties of the superficial biofilm layer determine the architecture of biofilms. *Soft matter* **2016**, *12*, 5718–5726.
- (45) Crocker, J.; Crocker, J.; Grier, D. Methods of digital video microscopy for colloidal studies. *J. Colloid Interface Sci.* **1996**, *179*, 298–310.
- (46) Bodin, A.; Backdahl, H.; Fink, H.; Gustafsson, L.; Risberg, B.; Gatenholm, P. Influence of Cultivation Conditions on Mechanical and Morphological Properties of Bacterial Cellulose Tubes. *Biotechnol. Bioeng.* **2007**, *97*, 425–434.
- (47) Hu, S. Q.; Gao, Y. G.; Tajima, K.; Sunagawa, N.; Zhou, Y.; Kawano, S.; Fujiwara, T.; Yoda, T.; Shimura, D.; Satoh, Y.; Munekata, M.; Tanaka, I.; Yao, M. Structure of bacterial cellulose synthase subunit D octamer with four inner passageways. *Proc. Natl. Acad. Sci. U. S. A.* **2010**, *107*, 17957–17961.
- (48) Janpetch, N.; Saito, N.; Rujiravanit, R. Fabrication of bacterial cellulose-ZnO composite via solution plasma process for antibacterial applications. *Carbohydr. Polym.* **2016**, *148*, 335–344.
- (49) Gromovykh, T. I.; Pigaleva, M. A.; Gallyamov, M. O.; Ivanenko, I. P.; Ozerova, K. E.; Kharitonova, E. P.; Bahman, M.; Feldman, N. B.; Lutsenko, S. V.; Kiselyova, O. I. Structural organization of bacterial cellulose: The origin of anisotropy and layered structures. *Carbohydr. Polym.* **2020**, *237*, 116140.

- (50) Qin, B.; Fei, C.; Bridges, A. A.; Mashruwala, A. A.; Stone, H. A.; Wingreen, N. S.; Bassler, B. L. Cell position fates and collective fountain flow in bacterial biofilms revealed by light-sheet microscopy. *Science* **2020**, *369*, 71–77.
- (51) Fu, L.; Zhang, Y.; Li, C.; Wu, Z.; Zhuo, Q.; Huang, X.; Qiu, G.; Zhou, P.; Yang, G. Skin tissue repair materials from bacterial cellulose by a multilayer fermentation method. *J. Mater. Chem.* **2012**, *22*, 12349–12357.
- (52) Huang, L.; Chen, X.; Nguyen, T. X.; Tang, H.; Zhang, L.; Yang, G. Nano-cellulose 3D-networks as controlled-release drug carriers. *J. Mater. Chem. B* **2013**, *1*, 2976–2984.
- (53) Zhou, L. L.; Sun, D. P.; Hu, L. Y.; Li, Y. W.; Yang, J. Z. Effect of addition of sodium alginate on bacterial cellulose production by *Acetobacter xylinum*. *J. Ind. Microbiol. Biotechnol.* **2007**, *34*, 483–489.
- (54) Cheng, K. C.; Catchmark, J. M.; Demirci, A. Effect of different additives on bacterial cellulose production by *Acetobacter xylinum* and analysis of material property. *Cellulose* **2009**, *16*, 1033–1045.
- (55) Kwandou, G. Characterization and control of biofilm and biofluid microstructure and rheology. Ph.D. thesis, University of New South Wales, Sydney, Australia, 2018.
- (56) Sankaran, J.; Tan, N. J.; But, K. P.; Cohen, Y.; Rice, S. A.; Wohland, T. Single microcolony diffusion analysis in *Pseudomonas aeruginosa* biofilms. *npj Biofilms and Microbiomes* **2019**, *5*, 1–10.
- (57) Remacha, E.; Friedrich, L.; Vermot, J.; Fahrback, F. O. How to define and optimize axial resolution in light-sheet microscopy: a simulation-based approach. *Biomed. Opt. Express* **2020**, *11*, 8–26.
- (58) Cai, L.-H.; Panyukov, S.; Rubinstein, M. Hopping diffusion of nanoparticles in polymer matrices. *Macromolecules* **2015**, *48*, 847–862.

- (59) Valentine, M. T.; Kaplan, P. D.; Thota, D.; Crocker, J. C.; Gisler, T.; Prud'homme, R. K.; Beck, M.; Weitz, D. A. Investigating the microenvironments of inhomogeneous soft materials with multiple particle tracking. *Phys. Rev. E* **2001**, *64*, 061506.
- (60) Chaudhuri, P.; Berthier, L.; Kob, W. Universal nature of particle displacements close to glass and jamming transitions. *Phys. Rev. Lett.* **2007**, *99*, 060604.
- (61) Gao, Y.; Kilfoil, M. L. Direct imaging of dynamical heterogeneities near the colloid-gel transition. *Phys. Rev. Lett.* **2007**, *99*, 1–4.
- (62) Wang, B.; Kuo, J.; Bae, S. C.; Granick, S. When Brownian diffusion is not Gaussian. *Nat. Mater.* **2012**, *11*, 481–5.
- (63) Stuhrmann, B.; Soares E Silva, M.; Depken, M.; MacKintosh, F. C.; Koenderink, G. H. Nonequilibrium fluctuations of a remodeling in vitro cytoskeleton. *Phys. Rev. E* **2012**, *86*, 1–5.
- (64) Lampo, T. J.; Stylianidou, S.; Backlund, M. P.; Wiggins, P. A.; Spakowitz, A. J. Cytoplasmic RNA-protein particles exhibit non-Gaussian subdiffusive behavior. *Biophys. J.* **2017**, *112*, 532–542.
- (65) Kegel, W. K.; van Blaaderen, A. Direct observation of dynamical heterogeneities in colloidal hard-sphere suspensions. *Science* **2000**, *287*, 290–293.
- (66) Wang, B.; Anthony, S. M.; Bae, S. C.; Granick, S. Anomalous yet brownian. *Proc. Natl. Acad. Sci. U. S. A.* **2009**, *106*, 15160–15164.
- (67) Weeks, E. R.; Crocker, J. C.; Levitt, A. C.; Schofield, A.; Weitz, D. A. Three-dimensional direct imaging of structural relaxation near the colloidal glass transition. *Science* **2000**, *287*, 627–631.

- (68) Ghazaryan, A.; Tsai, H. F.; Hayrapetyan, G.; Chen, W.-L.; Chen, Y.-F.; Jeong, M.-Y.; Kim, C.-S.; Chen, S.-J.; Dong, C.-Y. Analysis of collagen fiber domain organization by Fourier second harmonic generation microscopy. *J. Biomed. Opt.* **2012**, *18*, 031105.
- (69) Soumpasis, D. Theoretical analysis of fluorescence photobleaching recovery experiments. *Biophys. J.* **1983**, *41*, 95–97.
- (70) Carnell, M.; Macmillan, A.; Whan, R. *Methods in membrane lipids*; Springer, 2015; pp 255–271.
- (71) Hsu, M. N.; Wei, S. C.; Guo, S.; Phan, D. T.; Zhang, Y.; Chen, C. H. Smart hydrogel microfluidics for single-cell multiplexed secretomic analysis with high sensitivity. *Small* **2018**, *14*, 1–11.
- (72) Pedron, S.; Becka, E.; Harley, B. A. Spatially gradated hydrogel platform as a 3D engineered tumor microenvironment. *Adv. Mater.* **2015**, *27*, 1567–1572.
- (73) Deforest, C. A.; Tirrell, D. A. A photoreversible protein-patterning approach for guiding stem cell fate in three-dimensional gels. *Nat. Mater.* **2015**, *14*, 523–531.
- (74) Loebel, C.; Kwon, M. Y.; Wang, C.; Han, L.; Mauck, R. L.; Burdick, J. A. Metabolic labeling to probe the spatiotemporal accumulation of matrix at the chondrocyte–hydrogel interface. *Adv. Funct. Mater.* **2020**, *30*, 1–10.

Graphical TOC Entry

